Enhancement in photovoltaic performance of CZTS Thin-film solar cells through varying stacking order and sulfurization time

M. A. Olgar[1,2,*]

[1] *Department of Physics, Niğde Ömer Halisdemir University, Niğde, Turkey*
[2] *Nanotechnology Application and Research Center, Niğde Ömer Halisdemir University, Niğde, Turkey*

ABSTRACT

The CZTS samples were produced by a two-stage method, which includes deposition of Cu, Sn, Zn, and ZnS layers using magnetron sputtering to obtain CuSn/Zn/Cu and CuSn/ZnS/Cu stacks. The latter stage involves the sulfurization process of stacked films at 550 °C for varied sulfurization time (60, 90, 120, and 150 s) employing Rapid Thermal Processing (RTP) method to attain CZTS structure. The prepared CZTS thin films were analyzed utilizing several characterization methods. The energy-dispersive X-ray spectroscopy (EDX) measurements revealed that all sulfurized samples had Cu-poor and Zn-rich chemical composition. All samples showed that diffraction peaks belonged to pure kesterite CZTS phase subject to their XRD patterns. Besides, it was observed that the sulfurization time had a crucial effect on the crystal size of the samples. The Raman spectra of the samples verified the constitution of kesterite CZTS phase and it provides detection of some CTS-based secondary phases. The scanning electron microscopy (SEM) image of the films revealed that poly-crystalline surface structures were observable in all the samples. However, plate-like surface features were observed in some samples that may refer to CTS-based secondary phases depending on chemical composition. From 1.40 to 1.48 eV optical band gap values were obtained from $(\alpha h v)^2$ vs. photon energy (hv) plots. The Van der Pauw measurements exhibited that the CZTS samples produced employing CuSn/ZnS/Cu stack had lower resistivity ($\sim 10^{-3}$ Ω cm), higher carrier concentration values ($\sim 10^{21}$ cm^{-3}), and higher charge mobility. The solar cells prepared using the most promising CZTS samples employing CuSn/Zn/Cu and CuSn/ZnS/Cu precursor films revealed 1.95% and 3.10% conversion efficiencies, respectively.

Address correspondence to E-mail: mehmetaliolgar@ohu.edu.tr

🍃 Springer

1 Introduction

With increasing energy demand, the search for alternative energy sources to fossil fuels has accelerated recently. In this context, the interest in solar cells, which is one of the most important renewable energy sources, is increasing day by day. Thin-film solar cells have become a hot topic recently due to the low amount of material usage and high conversion efficiency. CdTe and Cu(In,Ga)Se$_2$ (CIGS) solar cells are leading structures in this field due to the their high cell performance [1, 2]. However, the scarce nature reserves of In and Ga elements and toxic property of Cd have led to the search for alternative materials to these materials. Cu$_2$ZnSnS$_4$ (CZTS) thin film is one of the most widely studied alternative semiconductor material for solving the aforementioned problems. It consists of plentiful and non-toxic raw materials. It also has p-type conductivity, 1.4–1.6 eV band gap, and high absorption coefficient ($> 10^4$ cm^{-1}) [3, 4]. All the aforementioned optical and electrical properties make this compound a strong candidate to an absorber layer in photovoltaic applications.

Although CZTS thin film has outstanding optical and electrical properties, the highest cell efficiency has been recorded to be 12.6% since 2014 [5]. According to Shockley–Queisser theoretical calculations, there is a potential to achieve efficiency above 30% in CZTS-based solar cells [6]. The reason for reported low conversion efficiency compared to the theoretical limit can be attributed to many reasons. However, one of the most important reason is the purity and crystalline quality of the absorber layer. Therefore, several different approaches were employed in the reported literature for the optimization crystalline quality of the absorber layer. The principal optimizations are based on growth parameters of the CZTS thin films. These optimizations consist of the composition of the film [7, 8], stacking order of precursor layers [9–12], sulfurization temperature and time [13–16], heating rate of the annealing process [17], and doping of the absorber layer [18–21]. In addition to these approaches, the graded-band structure approach is a widely used method recently in the literature. Taskesen et al. tried to obtain steep sulfur gradient in CZTSSe solar cells through H$_2$S-assisted rapid surface sulfurization. They achieved to introduce S/(S + Se) gradient in the absorber layer and observed that graded-band

structure has significant impact on device performance [22]. Among the aforementioned parameters and approaches, the stacking order of precursor layers and sulfurization time play a significant role on the properties of CZTS thin films. Liu et al. employed two different stacked films (ZnS/CuSn/Mo/SLG and CuSn/ZnS/Mo/SLG) by sputtering method. They observed that after the sulfurization process of precursor films, the CZTS thin films obtained using ZnS/CuSn/Mo/SLG showed a larger crystallite size, occurrence of less secondary phase, and higher conversion efficiency (5.22%). In addition, it was observed that the stacking order affects the conduction band offset (CBO) at CdS/CZTS heterojunction that improves the conversion efficiency directly [23]. It can be easily said that the stacking order of precursor films influences the crystalline quality of the absorber layer directly and it can also modify the band offset of the p–n junction and thus improve conversion efficiency.

Another important parameter is the reaction time of the sulfurization process. Akcay et al. prepared CZTS thin films by the sulfurization of co-sputtered precursor films employing various sulfurization time (10, 15, 20, and 25 min). They observed that the CZTS thin film sulfurized for 15 min demonstrated the best structural and morphological properties among the other CZTS samples [16]. Abdalbahi et al. prepared CZTS thin films by electrodeposition from metal precursors. Then, various sulfurization times (75, 90, 105, and 120 min) were used to investigate the impact of reaction time on the characteristic of CZTS structure. They showed that the CZTS samples sulfurized for 120 min had stoichiometric composition, purer, denser, and more compact structure. As understood from the performed studies, the sulfurization time has remarkable impact on the properties of CZTS thin films [24]. Overall, the stacking order and sulfurization parameters of precursor layers play a crucial role in crystalline quality of the CZTS absorber layer, thus affect conversion efficiency directly [9, 15, 25–28].

In this study, it is aimed to examine the impact of two important parameters together, stacking order and sulfurization time. To the best of my knowledge, this is the first study investigating the effect of sulfurization time employing Glass/CuSn/Zn/Cu and Glass/CuSn/ZnS/Cu stacked films. Optimizing sulfurization time subject to used stacked films will contribute to improving the cell efficiency and conversion more electrical energy.

In this context, two different stacking order (Glass/CuSn/Zn/Cu and Glass/CuSn/ZnS/Cu) and four short sulfurization times (60, 90, 120, and 150 s) were employed to find the more promising stacking order and more proper sulfurization time for the growth of CZTS thin films. The main purpose of obtaining CuSn alloy in the stacked films is to prevent Sn loss from the samples due to high vapor pressure of SnS phase [29]. The short sulfurization periods were selected since Rapid Thermal Processing (RTP) annealing method allows high ramping rate to the reaction temperature, thus reducing possible decomposition reactions during the growth of CZTS structure [30].

2 Experimental

Glass/CuSn/Zn/Cu and Glass/CuSn/ZnS/Cu stacked precursor samples were prepared by DC and RF magnetron sputtering using Cu, Sn, Zn, and ZnS targets. Prior to the deposition process, the glass substrates were cleaned in ultrasonic cleaner using acetone, isopropanol, and distilled water. The base pressure in the sputtering chamber was set to below 2×10^{-6} Torr and the operating pressure during the deposition process was set to 10^{-3} Torr. The Glass/CuSn/Zn/Cu stacked film was prepared as follows: (i) about 75% portion of Cu was deposited on substrate, (ii) Sn was deposited on Cu layer and annealed in sputtering chamber at 200 °C for 5 min to obtain Glass/CuSn structure, (iii) Zn was sputtered on Glass/CuSn, (iv) the rest portion of Cu ($\sim 25\%$) was deposited on Zn to form Glass/CuSn/Zn/Cu structure. A similar approach was carried out to prepare the other stacked film, Glass/CuSn/ZnS/Cu structure. Unlike the first stacking order films, ZnS layer was deposited in the structure instead of Zn layer. The schematic illustration of deposited precursor films with their thickness is shown in Fig. 1. The thicknesses of these layers were chosen according to the CZTS absorber layer thickness optimized in the reported literature [31, 32].

The precursor samples were fabricated with large size by sputtering method and then they were cut into small pieces for sulfurization process. The prepared stacked precursor films were then annealed in sulfur atmosphere using RTP method to obtain CZTS phase. All the annealing processes were conducted at 550 °C with 1 °C/s heating rate for 60, 90, 120, and 150 s of dwell time in sulfur atmosphere. The reason for choosing this sulfurization temperature is that the most promising temperature was found to be 550 °C in the temperature optimization study that was carried out earlier by own our research group [33]. The CZTS specimens were denoted according to the stacking order and their sulfurization time. The CZTS thin films obtained using elemental zinc (Zn), Glass/CuSn/Zn/Cu, were encoded as type "I," the CZTS samples prepared using the zinc sulfide (ZnS), Glass/CuSn/ZnS/Cu, were encoded as type "II" films. The nomination of prepared CZTS samples are shown in Table 1.

The X-ray diffraction (XRD) method was used with a CuK$_\alpha$ radiation source ($\lambda = 1.5405$ Å) to examine structural peculiarities of the prepared CZTS samples. The Raman spectroscopy method was utilized as a complementary technique in the structural characterization of the films using an excitation wavelength of 633 nm. The morphological structure and chemical composition were analyzed by scanning electron microscope (SEM) and energy-dispersive X-ray spectroscopy (EDX). The EDX spectroscopy measurements were taken from $125 \times 100~\mu m^2$ area so as to reveal chemical composition of the films more accurately. The optical properties of the CZTS samples were specified employing transmission measurement in the wavelength range of 600–1300 nm. The Van der Pauw method was used to investigate electrical properties of the films at room temperature. For this measurement, Ag paste dots of about 1 mm diameter were placed at the four corners of square samples. After analyses of CZTS thin films, the most promising CZTS films from both type of samples were selected for the fabrication of solar cell. For solar cell application, the same deposition procedure was applied for molybdenum-coated glass substrates (Glass/Mo) to obtain Glass/Mo/CuSn/Zn/Cu and Glass/Mo/CuSn/ZnS/Cu. Then, for solar cell structure, the upper layers (CdS, i-ZnO, AZO, and Al) were deposited on CZTS thin film sequentially. The CdS thin film (~ 60 nm) was deposited using Chemical Bath Deposition (CBD) method. The cadmium acetate dehydrate and thiourea were used as Cd and S sources, respectively. The 80 nm of i-ZnO and 300 nm AZO thin films were deposited by RF magnetron sputtering employing single sputtering targets of these materials. The complete solar cell structure was constructed by sputter deposition of aluminum

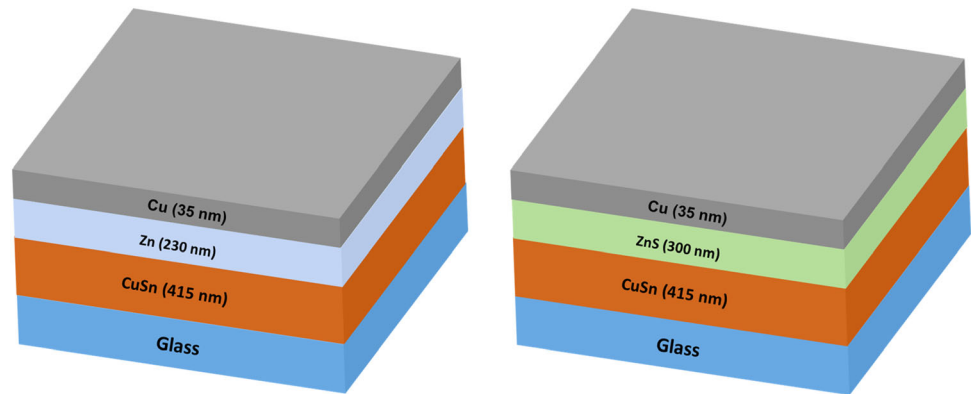**Fig. 1** Schematic illustration of the prepared precursor films

Table 1 Preparation parameters of the samples

Sample	Stacking order	Sulfurization
I-60	CuSn/Zn/Cu	550 °C, 60 s
I-90		550 °C, 90 s
I-120		550 °C, 120 s
I-150		550 °C, 150 s
II-60	CuSn/ZnS/Cu	550 °C, 60 s
II-90		550 °C, 90 s
II-120		550 °C, 120 s
II-150		550 °C, 150 s

(Al) contacts ($\sim$ 2 µm). The solar cells (1 $\times$ 1 cm^2) were characterized by J–V measurements taken under a 100 mW/cm^2 illumination employing solar simulator.

3 Results and discussion

3.1 EDX

The chemical composition (atomic percentage and atomic ratio) of type I and II precursor and CZTS samples is summarized in Table 2. Both types of precursor films had Cu-poor (Cu/(Zn + Sn) < 1) and Zn-rich (Zn/Sn > 1) chemical composition prior to the sulfurization process (see I precursor and II precursor in Table 2). After the sulfurization process of precursor films using various sulfurization time, chemical composition of all CZTS thin films exhibited Cu-poor and Zn-rich composition regardless of stacking order of precursor films and sulfurization time. The Cu-poor and Zn-rich chemical composition is the preferred property in CZTS thin-film solar cells by improving the p-type conductivity of the absorber

layer, enhancing the separation of electrons and holes, and reducing of recombination processes [34]. Therefore, it can be said that all CZTS thin films belong to the desired chemical composition after the sulfurization process. In addition, all CZTS samples were found to have enough sulfur content in the structure.

3.2 XRD

The XRD patterns of I-type CZTS samples are shown in Fig. 2.

All the patterns have dominated by peaks placed at around 2θ = 28.48°, 47.37°, and 56.22°, which are imputed to diffraction planes of kesterite CZTS phase irrespective of sulfurization time. The other peaks related to kesterite CZTS phase are signed in the patterns (JCPDS 00-26-0575). No any extra peaks related to undesirable phases were detected in these patterns.

The XRD pattern of II-type CZTS specimens are shown in Fig. 3. All patterns of II-type CZTS samples were dominated by the same peaks as observed in I-type CZTS samples and shown in the figure. As observed in I-type CZTS thin films, no undesired phase was detected in the XRD pattern of II-type CZTS samples.

The crystalline quality of type I and II CZTS thin films was compared by using full width at half-maximum (FWHM) value of (112) peak extracted from Figs. 2 and 3. The Scherrer formula is as below [30]:

$$D = \frac{K\lambda}{\beta \cos \theta}, \tag{1}$$

where D, K, λ, β, and θ correspond to crystallite size, Scherrer constant, wavelength of X-ray, full width at

Table 2 The composition of type I and II precursor and CZTS thin films

Specimen	Atomic (%)				Atomic ratio		
	% Cu	% Zn	% Sn	% S	Cu/(Zn + Sn)	Zn/Sn	S/metal
I precursor	45.24	30.48	24.30	–	0.83	1.25	–
I-60	20.67	14.15	12.49	52.7	0.78	1.13	1.11
I-90	20.49	13.86	12.15	53.5	0.79	1.14	1.15
I-120	20.62	14.18	12.07	53.13	0.79	1.17	1.13
I-150	20.73	14.14	12.24	52.89	0.79	1.16	1.12
II precursor	39.60	22.76	20.05	26.50	0.92	1.14	0.32
II-60	20.52	13.72	12.60	53.15	0.78	1.09	1.13
II-90	20.64	14.28	12.26	52.82	0.78	1.16	1.12
II-120	21.25	14.09	12.06	52.60	0.81	1.17	1.11
II-150	21.26	14.23	11.98	52.53	0.81	1.19	1.11
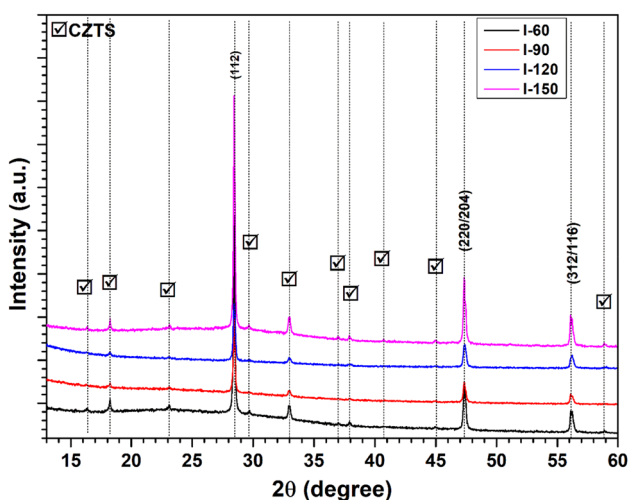
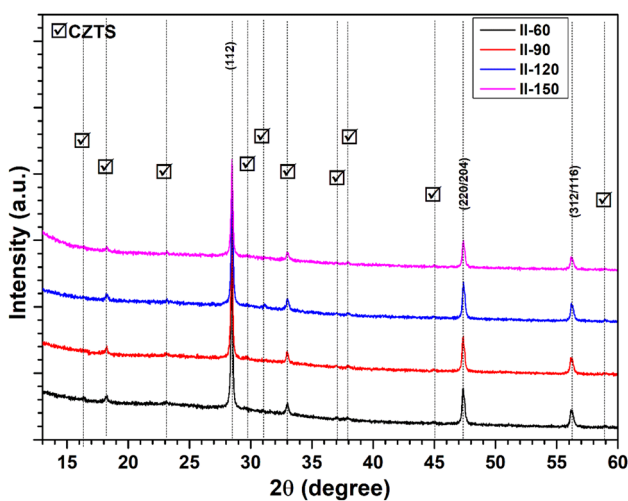**Fig. 2** X-ray diffraction patterns of I-type CZTS thin films

Fig. 3 The XRD patterns of II-type CZTS thin films

half-maximum (FWHM), and Bragg's angle, respectively. According to Scherrer formula, the crystallite

size is directly proportional with smaller FWHM value. Therefore, the smaller FWHM value means larger crystal size. The variation of FWHM values of type I and II CZTS thin films with respect to sulfurization time is shown in Fig. 4.

As shown in Fig. 4, the FWHM values varied from 0.14° to 0.20° (from 0.0024 rad to 0.0035 rad) in I-type CZTS thin films, from 0.15° to 0.16° (from 0.0026 rad to 0.0028 rad) in II-type CZTS specimens with ascending the sulfurization time. The crystallite size of the samples were calculated using Eq. (1) employing the FWHM values of the CZTS samples. From the calculations, the crystallite size of the I-type CZTS samples was found to be 61 nm, 53 nm, 43 nm and 61 nm, respectively, with increasing the sulfurization time. Similarly, these calculations were performed for II-type CZTS samples. The crystallite size of the CZTS samples were found to be 53 nm, 57 nm,
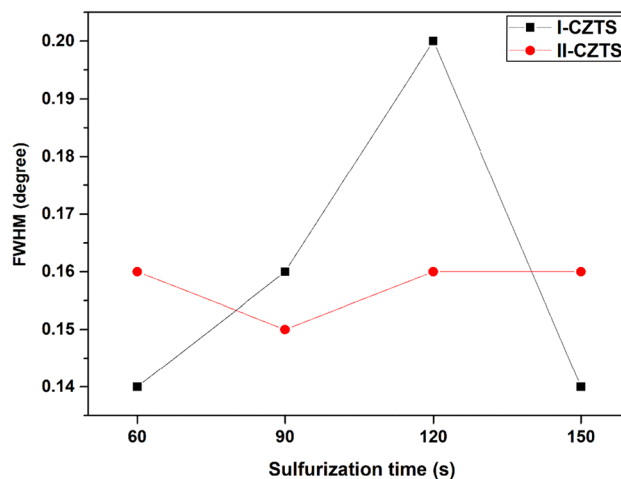

Fig. 4 FWHM value of preferential (112) peak of type I and II CZTS samples with respect to sulfurization time

53 nm, and 53 nm, respectively, subject to the increasing sulfurization time. It was observed that as the dwell time of the sulfurization increased in I-type CZTS thin films, the crystallite size of the films decreased. However, it was observed that the crystalline quality improved with sulfurization time over 120 s. Conversely, in II-type CZTS thin films, when the sulfurization time increased up to 90 s, the crystalline quality enhanced. It was observed that the dwell time above 90 s at the reaction temperature did not have positive impact on the crystalline quality of II-type CZTS thin films.

The difference in crystalline quality of CZTS samples stems from both stacking order and sulfurization time of precursor layers. This difference can be attributed to the formation reactions of the CZTS structure [35]. The use of ZnS layer instead of Zn in the growth stage may cause both a decrease in the formation reaction time and a change in crystalline quality. Overall, XRD patterns of CZTS samples demonstrated that kesterite CZTS phase formed in all samples without considering stacking order and sulfurization time. However, the I-60, I-150, and II-90 CZTS samples revealed more promising crystalline quality concerning crystallite size.

3.3 Raman spectroscopy

Raman spectroscopy measurements were taken to verify the occurrence of the kesterite CZTS phase and detect secondary phases that are indistinct in XRD measurement since it is well known that ZnS (05-0566) and Cu_2SnS_3 (01-089-4714) phases have resembling XRD patterns with kesterite CZTS structure. In this context, the Raman spectroscopy is the commonly used as subsidiary technique for the characterization of CZTS thin films.

Figure 5 illustrates the Raman spectra of I-type CZTS thin films. As it is clear, the Raman spectra of all films are curbed by a Raman band (~ 336 cm^{-1}) that is ascribed to one of the vibration modes of kesterite CZTS structure regardless of the sulfurization time [36].

The other vibration modes of the same phase are appointed at $\sim 253, 263, 287, 365$ cm^{-1} and signed in the figure. Apart from CZTS phase, some minor peaks placed at 300–303, 312–314, 317–318, 320, 348, and 353–354 cm^{-1} were found, which may be attributed to Cu–Sn–S (CTS)-based ternary phases such as $Cu_2SnS_3, Cu_2Sn_3S_7, Cu_3SnS_4$ [37–39]. However, it was
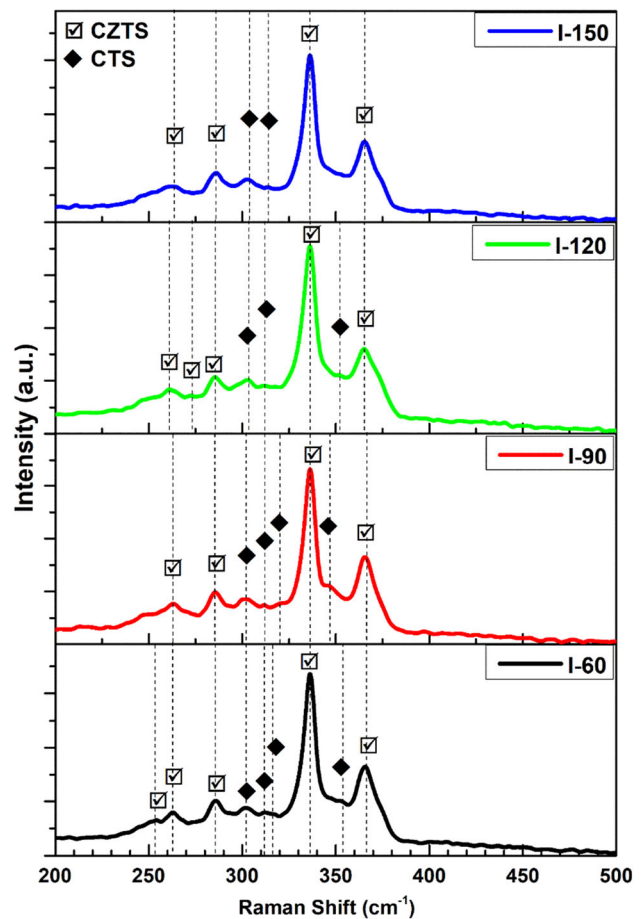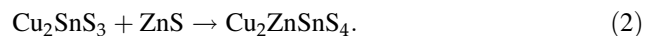

Fig. 5 Raman spectra of I-type CZTS samples

determined that the peaks of Cu–Sn–S-based phases decreased with increasing sulfurization time. This situation may refer to less CTS constitution in the structure of the films when increasing the sulfurization time. The constitution mechanism of CZTS is commonly reported as follows [35]:

$$Cu_2SnS_3 + ZnS \rightarrow Cu_2ZnSnS_4. \tag{2}$$

Therefore, decreasing the amount of Cu–Sn–S-based phases with increasing sulfurization time can be clarified by insufficient sulfurization time to obtain complete CZTS structure.

Figure 6 represents the Raman spectra of II-type CZTS samples. As observed in the figure, all the Raman spectra of II-type CZTS thin films are curbed by ~ 336 cm^{-1} peak that belongs to kesterite CZTS phase. The lower intense Raman bands belong to of the same phase are shown in the figure. Apart from CZTS phase, some minor peaks were detected at around 303, 312–314, and 348 cm^{-1}, which are attributed to Cu–Sn–S (CTS) phase as observed in
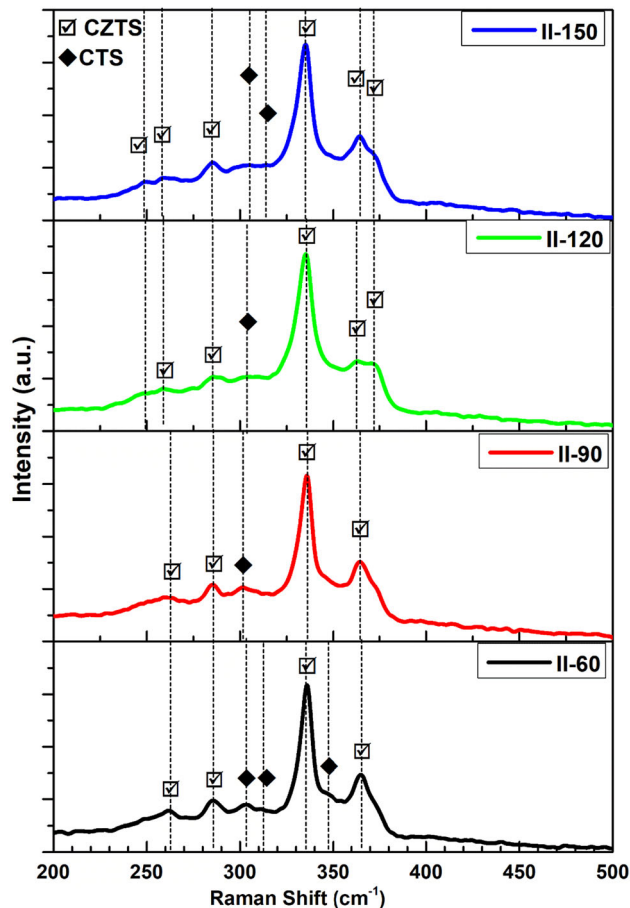
Fig. 6 Raman spectra of II-type CZTS thin films

type I CZTS films [40, 41]. As the sulfurization time increased up to 120 s, the peaks related to CTS phase decreased. It can be interpreted that the amount of CTS phase may decrease. Increasing the sulfurization time above 120 s may cause the constitution of more CTS phases in the structure with respect to II-90 and II-120 CZTS samples.

The occurrence of more CTS-based phases at sulfurization time above 120 s can be explained by reversible reaction of Eq. (2) [42]. It may be summarized that the use of ZnS precursor layer in place of Zn layer may accelerate the creation reaction of CZTS phase and make this kind of stack more proper for short sulfurization periods.

The presence of only CZTS and CTS phases in the Raman spectra of both types of samples does not mean that there is no ZnS phase in the structure of the films. The insufficient of the energy of the laser source used to excite the vibration modes of the ZnS phase makes it difficult to detect this phase.

Overall, it was achieved to produce CZTS phase irrespective of stacking order and sulfurization time in all samples regarding Raman spectroscopy. As compared to Raman spectra of I- and II-type CZTS thin films, I-150 and II-90 CZTS samples revealed less constitution of undesired phases among samples of the same type.

3.4 SEM

The top view of I-type CZTS thin films was examined by SEM and is shown in Fig. 7. SEM images of all I-type CZTS samples showed dense, non-uniform, and polycrystalline surface structure. However, it was observed that I-type CZTS samples had similar surface morphologies in pairs. While I-60 and I-90 had similar surface (Fig. 7 a, b), I-120 and I-150 CZTS thin films displayed similar surface morphology (Fig. 7 c, d). Plate-like surface features were observed in SEM image of I-60 and I-90 CZTS thin films. EDX point measurement of plate-like features showed that they had Zn-poor and Sn-rich (Zn/Sn = 0.4) chemical composition, which may sign the formation of Cu–Sn–S (CTS)-based phases. However, I-120 and I-150 CZTS thin films did not have such features.

This consequence is consistent with Raman spectroscopy measurements (see Fig. 5). It was predicted that more CTS phases should exist in of I-60 and I-90 CZTS specimens from Raman spectroscopy measurements.

Figure 8 represents the surface morphology of II-type CZTS thin films.

According to Fig. 8, all the specimens demonstrated dense, non-uniform, and polycrystalline surface structure, alike I-type CZTS samples. As observed in I-type CZTS thin films, the surface morphology similarity was observed in II-type CZTS samples in pairs. II-60 and II-90 CZTS samples and II-120 and II-150 CZTS samples share similar surface structure in pairs. Plate-like surface features were also observed in II-120 and II-150 CZTS samples. It means that CTS-based secondary phases formed more intensely on the surface of these samples. Such features were not observed in the surface of II-60 and II-90 CZTS thin films. The absence of possible CTS phase features on the surface of II-60 and II-90 CZTS samples produced at lower sulfurization times does not mean that this phase does not exist. It is predicted that the CTS phase might be formed in the bulk structure rather than the sample surface.
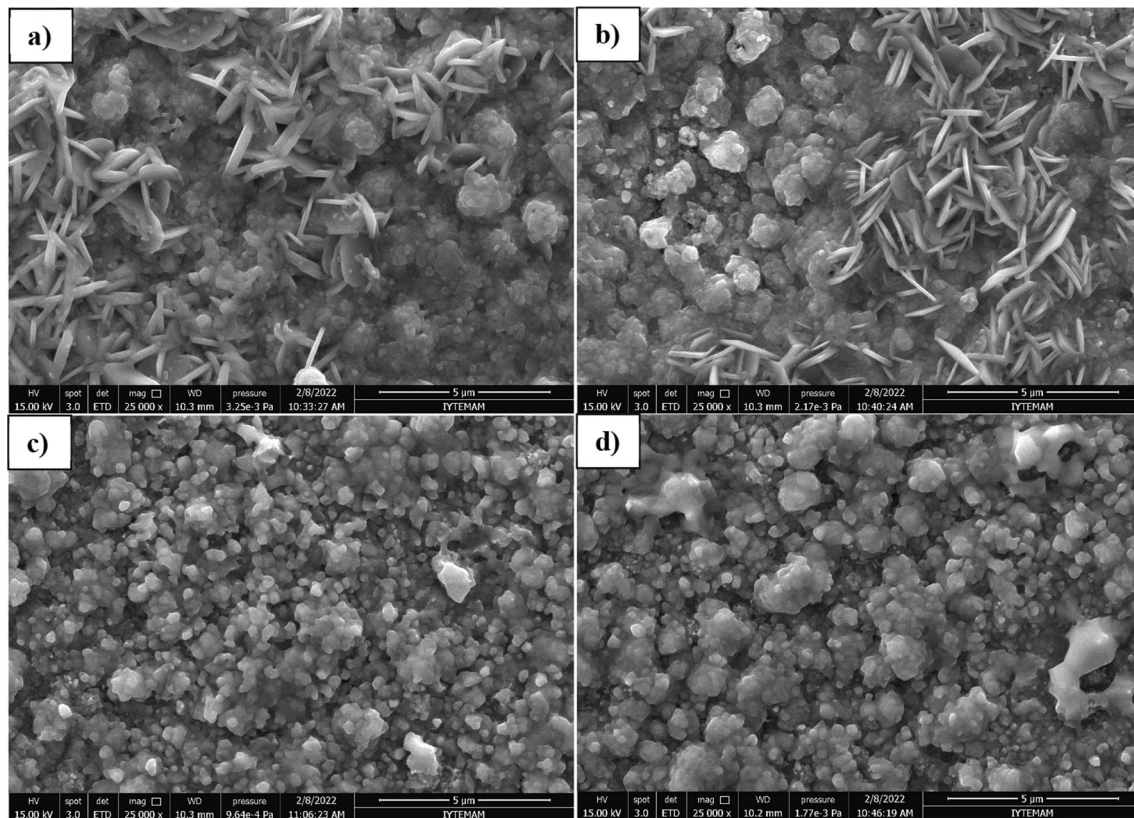
Fig. 7 SEM images of I-60 (**a**), I-90 (**b**), I-120 (**c**), and I-150 CZTS thin films

Overall, all the prepared CZTS thin films shared dense, non-uniform, and polycrystalline surface microstructure regardless of the stacking order and sulfurization time. The constitution of CTS-based undesired phases was observed in both types of the CZTS samples. Such creation was observed at earlier sulfurization time in I-type and at higher sulfurization time in II-type CZTS samples. The constitution at earlier time may indicate that formation reactions for CZTS structure are not completed due to short reaction time. The constitution at higher sulfurization time may sign to phase segregations in the structure [35, 43]. Therefore, higher sulfurization time in I-type and shorter sulfurization time in II-type CZTS thin films seem more suitable for the fabrication of CZTS thin films.

3.5 Optical and electrical properties

The optical band gap of type I and II CZTS samples was found utilizing Tauc plot [44]. The optical band gaps were estimated from extrapolating $(\alpha h v)^2$ versus $(h v)$ plots to intercept the axis of photon energy. Figure 9 presents $(\alpha h v)^2$ versus $(h v)$ plots of type I and

II CZTS thin films. The determined band gap of all the CZTS thin films is summarized in Table 3. As summarized in the table, the forbidden band gap values varied from 1.40 to 1.48 eV. The obtained band gap values are consistent with the reported literature [3, 45]. The variation in the forbidden energy range can be attributed to the differences in crystalline quality and chemical composition, and the formation of secondary phases results from these differences [46, 47]. In addition, it was observed that the plots do not drop to zero in the subgap region, especially in I-type CZTS thin films. This might be due to significant band tails extending into the band gap or parasitic absorption, e.g., due to Cu_2SnS_3 secondary phases [48]. This circumstance was not observed in the II-type CZTS specimens except for the II-150 CZTS specimen. It means that II-type CZTS thin films have purer band structure compared to I-type CZTS thin films.

The electrical properties of the CZTS samples were characterized using Van der Pauw method. According to the electrical characterization, all CZTS samples showed p-type electrical conductivity
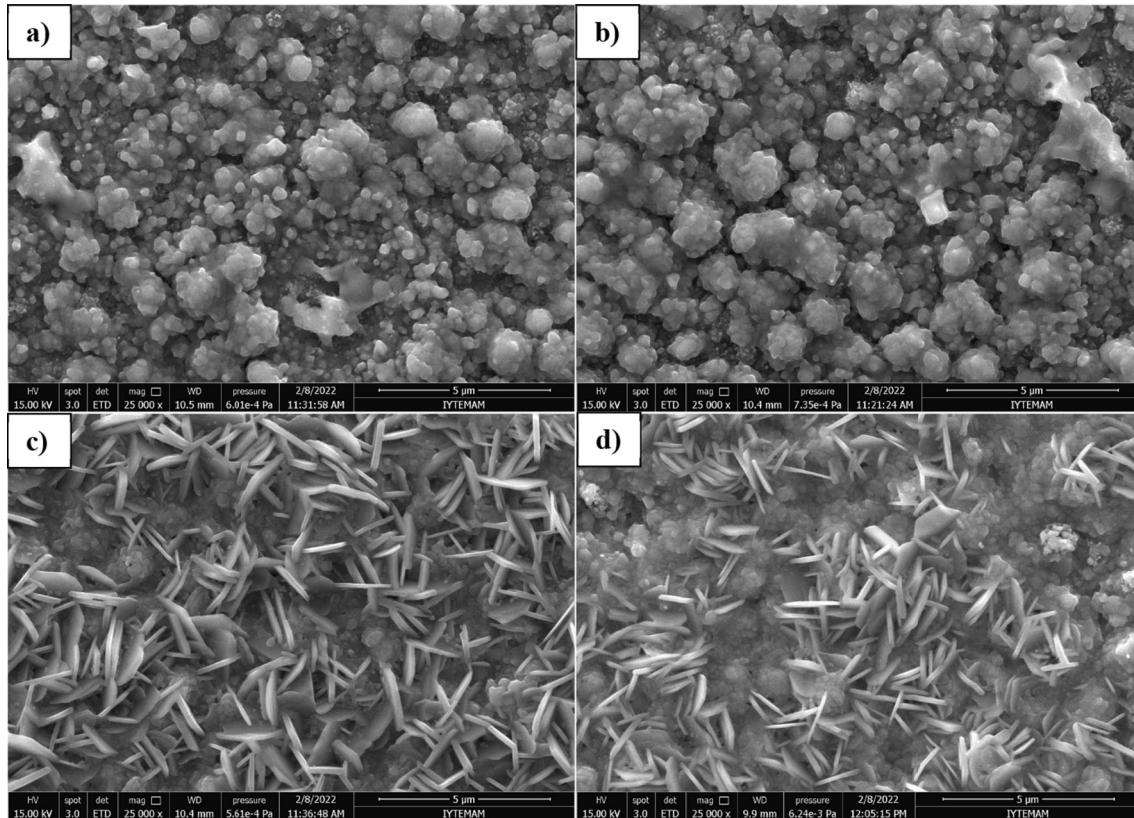
Fig. 8 SEM images of II-60 (**a**), II-90 (**b**), II-120 (**c**), and II-150 CZTS thin films

irrespective of the stacking order and sulfurization time. The other electrical properties (resistivity, carrier concentration, mobility) of the films are summarized in Table 4.

The Van der Pauw electrical measurement showed that the resistivity values of I-type CZTS thin films are on the order of 10^{-2} Ω.cm and II-type CZTS thin films are on the order of 10^{-3} Ω cm (see Table 4). Resistivity values of I-type CZTS samples varied from 1.1×10^{-2} to 2.3×10^{-2} Ω cm and it can be said that the resistivity values are very similar. On the other hand, resistivity values of II-type CZTS samples varied from 1.3×10^{-3} to 6.1×10^{-3} Ω cm that have lower resistivity values in point of I-type CZTS samples. The carrier concentration values were found in the range of 10^{20}–10^{21} cm^{-3}. The obtained results coincide with the literature [49]. Overall, the lowest resistivity and highest carrier concentration values were found as 1.3×10^{-3} Ω.cm and 1.4×10^{21} cm^{-3} with II-90 CZTS sample. In addition, the charge mobility of the samples varied from 0.36 to 8.54 cm^2/ V s. It was observed that the mobility values of charge carriers in II-type CZTS samples were higher than I-type CZTS samples. Therefore, it is possible to say that the II-type CZTS samples have a purer structure since the mobility is strongly dependent on microstructure and impurity of the films [50]. As a result of all the structural, optical, and electrical analyses made, it was observed that the II-90 sample showed superior properties than all the samples. However, in order to see the effect of the stacking order on cell performance, the I-150 sample, which has the best properties in I-type samples, and II-90 CZTS sample, which has the best properties in II-type samples, were selected for cell application.

3.5.1 Solar cell

Two kinds of solar cells were produced based on the performed analyses. The I-150 and II-90 CZTS absorber layers were selected for solar cell application since they presented the most promising properties. The complete solar cell structures of I-150 and II-90 CZTS-based cells are illustrated schematically in Fig. 10.
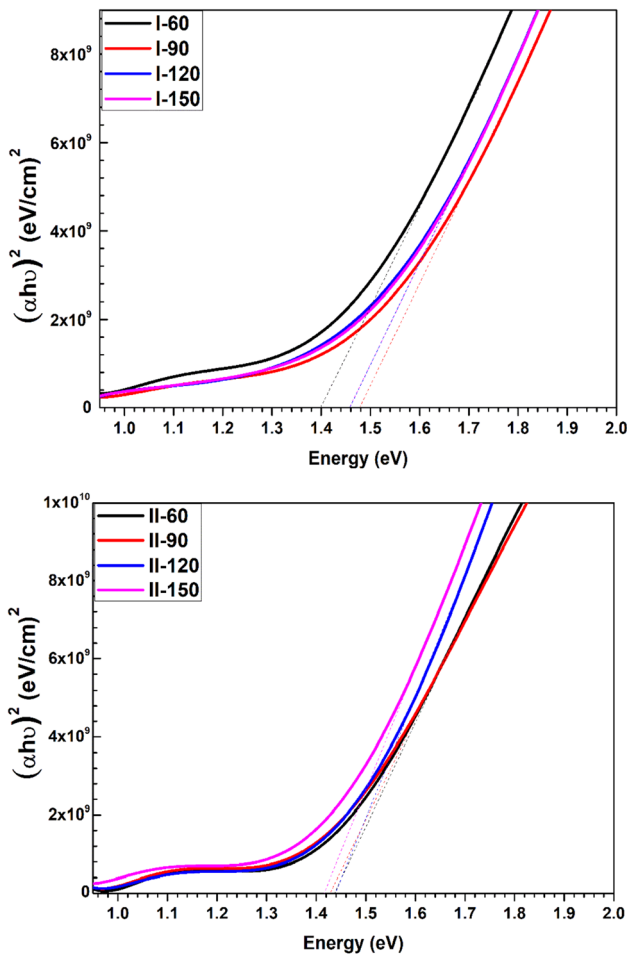
Fig. 9 Tauc plots for estimation of optical band gap of I and II-type CZTS thin films

Fig. 10 Schematic illustration of I-150 and II-90 type CZTS thin-film solar cells

As shown in Table 5, the solar parameters of II-90 CZTS thin-film solar cell exhibited superior properties. The short-circuit current density (J_{sc}), open-circuit voltage (V_{oc}), and fill factor (FF) enhanced from 26.4 to 27.9 mA/cm^2, 0.211 to 0.285 V, and 0.35 to 0.39 using type II-90 CZTS sample, respectively. As a result of these improvements, it was observed that the cell efficiency enhanced from 1.95 to 3.10%. However, all samples exhibited low V_{oc} that gives rise to low conversion efficiency. Based on the recent studies in the literature, it is observed that the cells produced in this study have low V_{oc} values com-

Table 3 Optical band gap values of I and II-type CZTS thin films

Sample	I-type CZTS samples				II-type CZTS samples			
	I-60	I-90	I-120	I-150	II-60	II-90	II-120	II-150
Eg (eV)	1.40	1.48	1.46	1.46	1.44	1.43	1.44	1.41

Table 4 Electrical properties of I and II-type CZTS thin films

Sample		I-type CZTS samples				II-type CZTS samples			
		I-60	I-90	I-120	I-150	II-60	II-90	II-120	II-150
Resistivity (Ω cm) $\times 10^{-2}$		1.1	2.1	2.3	1.8	0.33	0.13	0.34	0.61
Carrier concentration (cm^{-3}) $\times 10^{20}$		4.3	6.2	7.5	5.3	13	14	8.5	1.2
Mobility (cm^2/V s)		1.32	0.48	0.36	0.65	1.46	3.43	2.16	8.54

The current density (J)–voltage (V) graphs of I-150 and II-90 CZTS-based thin film solar cells are shown in Fig. 11. The solar cell parameters of I-150 and II-90 CZTS thin-film solar cells are summarized in Table 5.
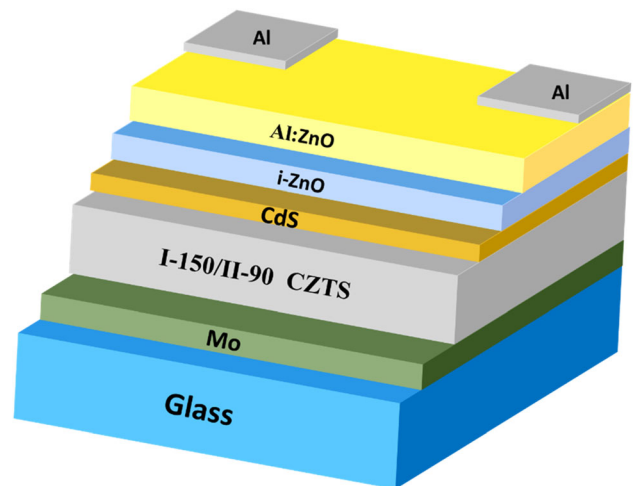
pared to reported works [51, 52]. The low V_{oc} in CZTS thin-film solar cells usually can be attributed to recombination mechanisms in CZTS bulk structure and at the CZTS/CdS interface [53]. The low V_{oc} can
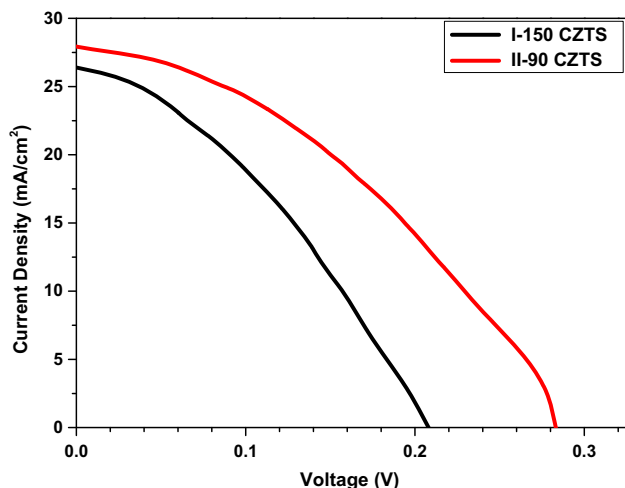
Fig. 11 Illuminated current density–voltage of I-150 and II-90 CZTS-based thin-film solar cells

Table 5 Solar cell parameters calculated from current density–voltage curves of I-150- and II-90-based CZTS thin films

Samples	J_{sc} (mA/cm^2)	V_{oc} (V)	FF (%)	η (%)
I-150	26.4	0.211	0.35	1.95
II-90	27.9	0.285	0.39	3.10

also be attributed to low-minority carrier lifetimes and diffusion lengths thanks to charge recombination [48]. Overall, although all cells suffer from low open-circuit voltages, it was observed that the CuSn/ZnS/Cu stacked precursor film is more proper than the CuSn/Zn/Cu stacked precursor film for CZTS-based thin-film solar cells.

4 Conclusion

In this study, CZTS samples were produced by two-stage technique comprising the deposition of Cu, Sn, Zn, and ZnS layers by sputtering method to form CuSn/Zn/Cu (I-type) and CuSn/ZnS/Cu (II-type) precursor films, which was followed by sulfurization at 550 °C for varied sulfurization time (60, 90, 120, and 150 s). After the sulfurization process through varied sulfurization time, all CZTS samples displayed Cu-poor and Zn-rich composition that is desirable for photovoltaic applications. All the XRD patterns displayed pure kesterite CZTS structure irrespective of the stacking order of precursor films

and sulfurization time. According to the FWHM values, 60 and 150 s sulfurization time in CuSn/Zn/Cu stack (I-type) and the 90 s sulfurization time in CuSn/ZnS/Cu stack exhibited a more desired crystallite size. The Raman spectra of the samples justified the constitution of kesterite CZTS phase in all the samples and some CTS phases. The SEM image of the samples demonstrated the creation of dense polycrystalline surface structure. In addition, CTS phases were observed as plate-like surface features. The optical band gap of the films was determined between 1.40 and 1.48 eV. The electrical properties of the films showed p-type conductivity regardless of the growth parameters and the II-type samples exhibited more desired electrical properties that are lower resistivity, higher carrier concentration, and higher mobility. The solar cells prepared using I-150 and II-90 CZTS films showed that type II precursor films (CuSn/Zn/Cu) exhibited better short-circuit current density, open-circuit voltage, and conversion efficiency with 27.9 mA/cm^2, 0.285 V, and 3.10%, respectively. Overall, considering all the measurements and performance of solar cell, the II-90 CZTS thin film that was prepared using CuSn/ZnS/Cu and 90 s of sulfurization time showed the most promising results. However, further investigations have already been in progress to boost the V_{oc} in the cells.

References

1. M. Nakamura, K. Yamaguchi, Y. Kimoto, Y. Yasaki, T. Kato, H. Sugimoto, IEEE J. Photovolt. **9**, 1863–1867 (2019)
2. M. Green, E. Dunlop, J. Hohl-Ebinger, M. Yoshita, N. Kopidakis, X. Hao, Prog. Photovolt. Res. Appl. **29**, 3–15 (2021)
3. H. Katagiri, N. Sasaguchi, S. Hando, S. Hoshino, J. Ohashi, T. Yokota, Sol. Energy Mater. Sol. Cells **49**, 407–414 (1997)
4. H. Katagiri, N. Ishigaki, T. Ishida, K. Saito, Jpn. J. Appl. Phys. **40**, 500–504 (2001)

5. W. Wang, M.T. Winkler, O. Gunawan, T. Gokmen, T.K. Todorov, Y. Zhu, D.B. Mitzi, Adv. Energy Mater. **4**, 1301465 (2014)

6. W. Shockley, H.J. Queisser, J. Appl. Phys. **32**, 510–519 (1961)

7. M.A. Olgar, A. Altuntepe, S. Erkan, R. Zan, J. Mol. Struct. **1230**, 129922 (2021)

8. O. Vigil-Galán, M. Espíndola-Rodríguez, M. Courel, X. Fontané, D. Sylla, V. Izquierdo-Roca, A. Fairbrother, E. Saucedo, A. Pérez-Rodríguez, Sol. Energy Mater. Sol. Cells **117**, 246–250 (2013)

9. N. Thota, M. Gurubhaskar, M.A. Sunil, P. Prathap, Y.V. Subbaiah, A. Tiwari, Appl. Surf. Sci. **396**, 644–651 (2017)

10. H. Araki, A. Mikaduki, Y. Kubo, T. Sato, K. Jimbo, W.S. Maw, H. Katagiri, M. Yamazaki, K. Oishi, A. Takeuchi, Thin Solid Films **517**, 1457–1460 (2008)

11. H. Yoo, J. Kim, Thin Solid Films **518**, 6567–6572 (2010)

12. S.W. Shin, S.M. Pawar, C.Y. Park, J.H. Yun, J.H. Moon, J.H. Kim, J.Y. Lee, Sol. Energy Mater. Sol. Cells **95**, 3202–3206 (2011)

13. K. Maeda, K. Tanaka, Y. Fukui, H. Uchiki, Jpn J. Appl. Phys. **50**, 01BE10 (2011)

14. H. Yoo, J.H. Kim, L.X. Zhang, Curr. Appl. Phys. **12**, 1052–1057 (2012)

15. H. Guan, H.L. Shen, C. Gao, X.C. He, J. Mater. Sci.: Mater. Electron. **24**, 2667–2671 (2013)

16. N. Akcay, T. Ataser, Y. Ozen, S. Ozcelik, Thin Solid Films **704**, 138028 (2020)

17. J. Ge, Y.H. Wu, C.J. Zhang, S.H. Zuo, J.C. Jiang, J.H. Ma, P.X. Yang, J.H. Chu, Appl. Surf. Sci. **258**, 7250–7254 (2012)

18. G. Sai Gautam, T.P. Senftle, E.A. Carter, Chem. Mater. **30**, 4543–4555 (2018)

19. C.A. Ava, Y.S. Ocak, S. Asubay, O. Celik, Opt. Mater. **121**, 111565 (2021)

20. Z. Su, W. Li, G. Asim, T.Y. Fan, L.H. Wong, Cation substitution of CZTS solar cell with> 10% efficiency, 2016 IEEE 43rd Photovoltaic Specialists Conference (PVSC), IEEE, 2016, pp. 0534–0538

21. T. Sanchez, E. Regalado-Pérez, X. Mathew, M. Sanchez, Y. Sanchez, E. Saucedo, N. Mathews, Sol. Energy Mater. Sol. Cells **198**, 44–52 (2019)

22. T. Taskesen, D. Pareek, D. Hauschild, A. Haertel, L. Weinhardt, W. Yang, T. Pfeiffelmann, D. Nowak, C. Heske, L. Gütay, Rsc Adv. **11**, 12687–12695 (2021)

23. X. Liu, J. Guo, R. Hao, Q. Zhao, F. Chang, L. Wang, B. Liu, Y. Li, K. Gu, Sol. Energy **183**, 285–292 (2019)

24. A. Aldalbahi, E. Mkawi, K. Ibrahim, M. Farrukh, Sci. Rep. **6**, 1–9 (2016)

25. C. Kim, S. Hong, Mol. Cryst. Liq. Cryst. **617**, 179–185 (2015)

26. X. Xu, S.R. Wang, X. Ma, S. Yang, Y.B. Li, Z. Tang, J. Mater. Sci.: Mater. Electron. **29**, 19137–19146 (2018)

27. M.P. Suryawanshi, S.W. Shin, U.V. Ghorpade, K.V. Gurav, C.W. Hong, P.S. Patil, A.V. Moholkar, J.H. Kim, J. Alloy Compd. **671**, 509–516 (2016)

28. P.K. Kannan, S. Chaudhari, S.R. Dey, Thin Solid Films **649**, 81–88 (2018)

29. V. Piacente, S. Foglia, P. Scardala, J Alloy Compd **177**, 17–30 (1991)

30. A. Fairbrother, L. Fourdrinier, X. Fontane, V. Izquierdo-Roca, M. Dimitrievska, A. Perez-Rodriguez, E. Saucedo, J. Phys. Chem. C **118**, 17291–17298 (2014)

31. B. Vermang, Y. Ren, O. Donzel-Gargand, C. Frisk, J. Joel, P. Salome, J. Borme, S. Sadewasser, C. Platzer-Björkman, M. Edoff, IEEE J. Photovolt. **6**, 332–336 (2015)

32. P. Prabeesh, V. Sajeesh, I.P. Selvam, M.D. Bharati, G.M. Rao, S. Potty, Sol. Energy **207**, 419–427 (2020)

33. M. Olgar, A. Sarp, A. Seyhan, R. Zan, Renew. Energy **179**, 1865–1874 (2021)

34. S. Chen, A. Walsh, X.G. Gong, S.H. Wei, Adv. Mater. **25**, 1522–1539 (2013)

35. F. Hergert, R. Hock, Thin Solid Films **515**, 5953–5956 (2007)

36. M. Dimitrievska, A. Fairbrother, X. Fontane, T. Jawhari, V. Izquierdo-Roca, E. Saucedo, A. Perez-Rodriguez, Appl. Phys. Lett. **104**, 021901 (2014)

37. M.A. Olgar, Superlattice Microstruct. **138**, 106366 (2020)

38. P.A. Fernandes, P.M.P. Salome, A.F. da Cunha, J. Alloy Compd. **509**, 7600–7606 (2011)

39. Y.C. Dong, J. He, X.R. Li, Y. Chen, L. Sun, P.X. Yang, J.H. Chu, J. Alloy Compd. **665**, 69–75 (2016)

40. T. Raadik, M. Grossberg, J. Krustok, M. Kauk-Kuusik, A. Crovetto, R.B. Ettlinger, O. Hansen, J. Schou, Appl. Phys. Lett. **110**, 261105 (2017)

41. Y. Zhao, X.X. Han, B. Xu, C. Dong, J.S. Li, X.B. Yan, J. Mater. Sci.: Mater. Electron. **30**, 17947–17955 (2019)

42. J.J. Scragg, T. Kubart, J.T. Watjen, T. Ericson, M.K. Linnarsson, C. Platzer-Bjorkman, Chem. Mater. **25**, 3162–3171 (2013)

43. A. Redinger, D.M. Berg, P.J. Dale, S. Siebentritt, J. Am. Chem. Soc. **133**, 3320–3323 (2011)

44. J. Tauc, Mater. Res. Bull. **3**, 37–46 (1968)

45. R. Deokate, R. Kate, S. Bulakhe, J. Mater. Sci.: Mater. Electron. **30**, 3530–3538 (2019)

46. C. Malerba, F. Biccari, C.L.A. Ricardo, M. Valentini, R. Chierchia, M. Muller, A. Santoni, E. Esposito, P. Mangiapane, P. Scardi, A. Mittiga, J. Alloy Compd. **582**, 528–534 (2014)

47. A.V. Moholkar, S.S. Shinde, G.L. Agawane, S.H. Jo, K.Y. Rajpure, P.S. Patil, C.H. Bhosale, J.H. Kim, J. Alloy Compd. **544**, 145–151 (2012)

48. M.A. Olgar, J. Klaer, R. Mainz, L. Ozyuzer, T. Unold, Thin Solid Films **628**, 1–6 (2017)
49. A. Tang, Z. Li, F. Wang, M. Dou, W. Mao, J. Mater. Sci.: Mater. Electron. **29**, 7613–7620 (2018)
50. S. Zhou, R. Tan, X. Jiang, X. Shen, W. Xu, W. Song, J. Mater. Sci.: Mater. Electron. **24**, 4958–4963 (2013)
51. H. Bencherif, Sol. Energy **238**, 114–125 (2022)
52. Z. Zhi, S. Wang, L. Huang, J. Li, X. Xiao, Mater. Sci. Semicond. Process. **144**, 106592 (2022)
53. S. Siebentritt, Thin Solid Films **535**, 1–4 (2013)